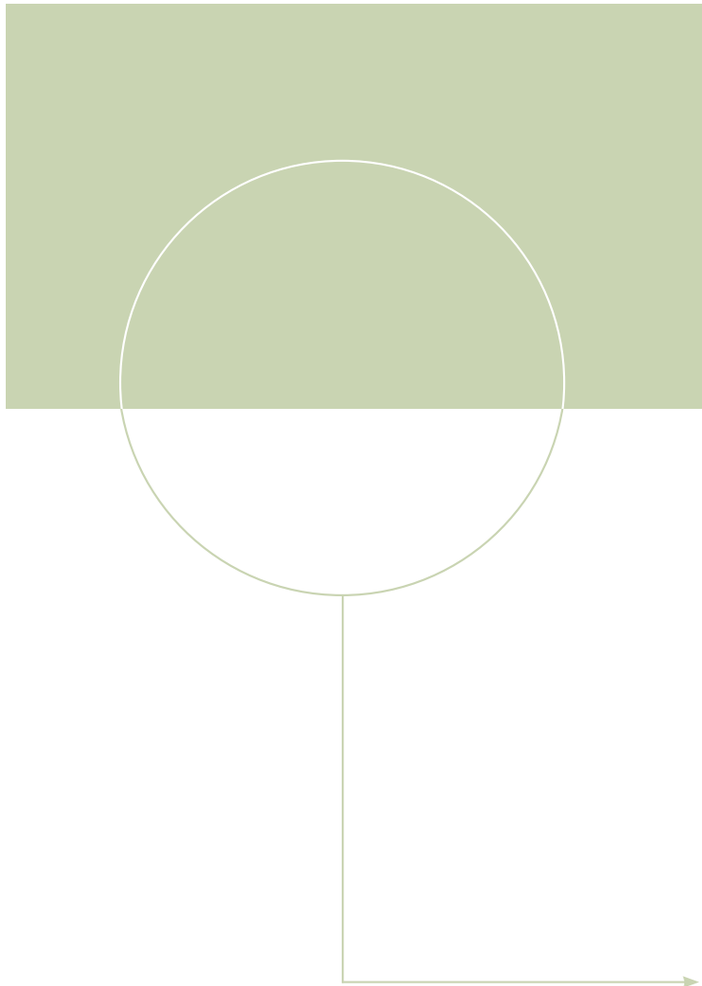

Master's thesis

2019

Mohammed Ettayebi

NTNU
Norwegian University of
Science and Technology
Faculty of Engineering
Department of Geoscience and Petroleum

Mohammed Ettayebi

Time-Domain Sensitivity Analysis Comparison of Two CSEM Methods

June 2019

NTNU
Norwegian University of
Science and Technology

NTNU
Norwegian University of
Science and Technology

NTNU

Norwegian University of
Science and Technology

Time-Domain Sensitivity Analysis Comparison of Two CSEM Methods

Mohammed Ettayebi

Petroleum Geoscience and Engineering
Submission date: June 2019
Supervisor: Rune Mittet
Co-supervisor: Jan Petter Morten

Norwegian University of Science and Technology
Department of Geoscience and Petroleum

ABSTRACT

Time-domain sensitivities of two different CSEM configurations have been investigated and compared. The first configuration combines vertical transmitters and vertical receivers, while the second considers horizontal transmitters and horizontal receivers. Typical frequency-domain CSEM experiments with horizontal transmitters and receivers have been used in many years. However, theory shows that deep resistive targets can better be detected and imaged if vertical transmitters and receivers were to be combined. Additionally, it is claimed that the airwave effect can be minimized if the time-domain is considered instead of the usual frequency-domain. These claims are investigated further, by simulating time-domain 3D electric fields in plane layer models generated by two different acquisition configurations, while considering experimental uncertainty. The time-domain electric fields are further employed to study and compare the sensitivity of each configuration to thin resistive targets in shallow and deep water environments. This was done by firstly modeling the EM responses in the frequency-domain. Then, the modeled responses were Fourier transformed to time-domain by the use of digital filters. The applied time-domain code uses a step-off waveform current, implying that the primary field is insignificant in the near offsets.
Regardless of the water depth, the vertical configuration shows higher sensitivities than the horizontal when the offset is 500 m and the resistive target is not buried deeper than 2000 m. However, burying the target deeper to 3000 m makes the situation water depth dependent, where the vertical configuration is the only method enabling target imaging in deep waters. The vertical configuration shows obvious weaknesses with larger offset, where target imaging is only feasible for shallow targets.
At the far offset in shallow waters, the airwave effect is understandably encountered for the horizontal configuration. However, the deepest target at 4000 m can still be successfully imaged, simply by reducing the experimental uncertainty. This implies that in deep waters, the same target can be imaged at mid-offsets, and a reasonable degree of detectability can be achieved at far offsets.

INTRODUCTION

Marine CSEM is about measuring subsurface resistivities from the seabed, with the fundamental acquisition principles being quite similar to what is typically done in Ocean Bottom Seismic (OBS), in the sense that both an active source and a receiver are required to conduct an EM experiment. A historical overview of the method is given by Constable (2010).

Being able to detect and image large-scale resistivity anomalies from high saturations of petroleum, marine CSEM sounding has gained increasing popularity, and hence application since its birth in 2000 (Ellingsrud et al., 2002). The latter of which has lead to the development of alternative acquisition configurations by which the experiment can be conducted. Two of these configurations are currently receiving attention in the commercial markets. The first uses vertical transmitters and vertical receivers (V-V) in the time-domain, whilst the second, which is the most widespread, combines horizontal transmitters and horizontal receivers (H-H) in the frequency-domain. Initially, all CSEM measurements are recorded in the time-domain. Subsequently, and depending on the waveform of the transmitted electric current, the recorded data can either remain in the time-domain or be transformed to the

frequency-domain . In the frequency-domain, the emitted electric current is a square wave, and the recorded response can be decomposed to represent each and every frequency constituting the frequency band. On the other hand, in the time-domain, the transient response is measured after the transmitter current in turned off, allowing us to represent amplitude variation with time.

Typical CSEM measurements with horizontal receivers and transmitters suffer from the weak attenuation of the EM signal propagating through the air layer known as the airwave at large offsets. This is especially true in shallow water environments (water depths less than 300 m), where this airwave effect becomes more prominent, masking the diagnostic resistor signature, and making the detection of thin targets more of a challenge. On the other hand, theory shows that the vertical configuration of transmitter and receiver antennas in the time-domain produces no airwave and is sensitive to deep resistive layers. Weiss (2007) showed that one possible way to handle the airwave effect in shallow waters is by using time-domain data instead of the usual frequency-domain data. The vertical configuration is supported by the work of Holten et al. (2009) and Chave and Cox (1982), showing that the vertical electric current emanated from a vertical electric dipole (VED) produces pure TM mode fields. In the TM mode, the vertical component of the magnetic field H_z is zero, while the vertical electric field component E_z is present, and due to the boundary conditions between water and air no airwave is generated. Constable and Weiss (2006) proved that the responses from a vertical electric field are more sensitive to the edges of a sub-seafloor resistor, being more convenient to map the lateral extent of thin resistive layers, than measurements done by receivers measuring the horizontal electric field component. Additionally, this study is also motivated by the work of Haland et al. (2012), who has shown that the horizontal electric field is more vulnerable to electromagnetic noise around the ocean wave frequencies than the vertical component, making it interesting to directly compare the two techniques, but now in the time-domain.
Unfortunately, each technique has its own shortcomings, and vertical electric fields measured by vertical receivers is not an exception. The amplitude response of vertical electric fields can be orders of magnitude smaller than the horizontal one (Holten et al., 2009), introducing the possibility of the vertical electric field to be overprinted by the horizontal component. Hunziker et al. (2011) showed that source tilt angles as small as 0.05° can give rise to the airwave composing 20% of the total recorded signal. This stipulates stringent requirements to the verticality of the acquisition system in the sense that the transmitter and receiver antennas should be as vertical as possible, with minimal tilt angles.

Cuevas and Alumbaugh (2011) have also looked into the differences between time-domain and frequency-domain EM fields due to a vertical or horizontal electric dipole excitation. However, theory versus experimental limitations incorporated in experimental uncertainty were not considered in their research.
The intention with this work is to model and study electric fields generated by two different acquisition configurations in the time-domain, while considering the experimental uncertainty. The first is a vertical transmitter vertical receiver, V-V, configuration, while the second is a horizontal transmitter horizontal receiver, H-H, configuration. To achieve that, numerical models simulating a 1D plane layered earth consisting of a water layer, a top formation, a thin horizontal HC reservoir, a bottom formation and a basement were constructed, and are initially modeled in the frequency-domain. Then, the modeled responses are Fourier transformed to the time-domain by the application of digital filters. This implies

that the initial code applied in this 1D modeling is in the frequency-domain, which is then transformed to the time-domain. This time-domain code uses a step-off waveform type, which implies that the transient responses are measured after the transmitter is switched off, ensuring that the primary field is insignificant in the near offset.

By drawing on the work done by Mittet and Morten (2012), the main objective of this research is to use the modeled time-domain series to investigate and compare the sensitivity of each method to thin resistive targets buried at different burial depths in shallow and deep water environments, and subsequently study the key parameters that can increase this sensitivity. Simultaneously, this sensitivity is also used to determine which configuration that best allows for detecting and imaging of the modeled resistive targets.
Mittet and Morten (2012) present and develop a formalism that aims to scrutinize the frequency-domain sensitivity of marine CSEM methods applied in hydrocarbon exploration defined as

$$Sensitivity(\omega) = \frac{\left|F_{Target} - F_{Background}\right|}{\delta F_{Target}}, \tag{1}$$

where $\omega = 2\pi f$ is the angular frequency and F could denote either the electric or magnetic field. The quantity $F_{Target} - F_{Background}$ is the "scattered or anomalous" field, i.e., the amplitude difference introduced by inserting a target into the initial background model. As for δF_{Target}, this represents a frequency-domain approximation to inherent data uncertainties pertaining to different acquisition parameters, and is given by,

$$\delta F_{Target}(\omega) = \sqrt{|\alpha E|^2 + |\eta|^2}. \tag{2}$$

The first term on the right-hand side of equation (2) stands for the relative uncertainty, i.e., the uncertainty constant α that scales with the electric field or its partial derivatives with respect to the different acquisition parameters. The second term η includes contributions from the ambient noise. Note that the uncertainty contribution raising from the verticality of the transmitter and receiver antennas has been neglected in this work, which if included could make the V-V configuration less favorable compared to the H-H.

The ratio in equation (1) decides to what extent it is possible to capture more resistivity information about the subsurface. According to Mittet and Morten (2012), this metric represents the best case scenario when the initial model does not contain any information about the resistive target. Hence, this ratio is used in the time-domain to investigate and compare the sensitivity behaviors of the two techniques to varying water depths, offsets, target burial depths and relative uncertainties.

THEORY

Time-domain responses

This research is based on the work done by Løseth and Ursin (2007) on frequency-domain EM plane layer earth modeling. An overview of the historical development of the marine controlled-source electromagnetic methods for hydrocarbon exploration is given by Constable and Srnka (2007).
In this research, 3D electric fields have been forward simulated in plane layer models. The code used in this work is a frequency-domain code simulating electric fields in the frequency-domain, which are then transformed to time-domain by the methods presented in this section. These time-domain responses are then used to study the sensitivity of each configuration to thin resistive targets.

Time-domain electric field components $E_i(t)$ due to a transmitter at position $\bar{x_s}$ and measured by a receiver at positions $\bar{x_r}$ can be obtained by,

$$E_i(\bar{x_r}, t|\bar{x_s}) = \int_0^{t^+} dt' \widetilde{G}_{ik}(\bar{x_r}, t - t'|\bar{x_s}) J_k(t'), \tag{3}$$

where $\widetilde{G}_{ik}$ is the electric field Green's function for an extended source and $J_k(t')$ represents the electric current amplitude. Indices i and k represent the different spatial directions of the receiver and source respectively.

The initial stage is to model frequency-domain point source Green's function components $G_{ik}(\bar{x_r}, \omega|\bar{x_s})$ for a given angular frequency $\omega = 2\pi f$. Subsequently, and since two different source-receiver configurations are to be analyzed in this case, the $\widetilde{G}_{ik}$ will be dependent on that, where in the H-H configuration:

$$\widetilde{G}_{xx}(\bar{x_r}, \omega|x_s, 0, z_s) = \int_{x_s - \frac{L}{2}}^{x_s + \frac{L}{2}} dx'_s G_{xx}(\bar{x_r}, \omega|x'_s, 0, z_s). \tag{4}$$

Similarly, the Green's function in the V-V configuration is given by,

$$\widetilde{G}_{zz}(\bar{x_r}, \omega|x_s, 0, z_s) = \int_{z_s - \frac{L}{2}}^{z_s + \frac{L}{2}} dz'_s G_{zz}(\bar{x_r}, \omega|x_s, 0, z'_s). \tag{5}$$

Here, L is the transmitter length, and $\bar{x_s} = (x_s, 0, z_s)$ represents the source's center spatial coordinates. $\widetilde{G}_{ik}(\bar{x_r}, \omega|\bar{x_s})$ are the Green's function components representing finite length source distributions in the frequency-domain, where all the contributions from the different point sources have been summed up over the transmitter length L.

By applying a Fourier transform to $\widetilde{G}_{xx}(\omega)$ and $\widetilde{G}_{zz}(\omega)$ from equations (4) and (5), time-domain impulse responses $\widetilde{G}_{ik}(t)$ can be obtained,

$$\widetilde{G}_{ik}(t) = \frac{1}{2\pi}\int_{-\infty}^{\infty} d\omega \widetilde{G}_{ik}(\omega)e^{-i\omega t}. \tag{6}$$

Application of the Fourier transform shown by equation (6) to frequency-domain EM measurements can be computationally expensive, requiring numerous evaluations to achieve an accurate response. Thus, the majority of EM modeling codes in use today employ the digital filter method suggested by Ghosh (1971). Werthmüller et al. (2018) provided a code based on digital filters, that can be used to transform frequency-domain responses to time-domain. The application of digital filters to estimate the time-domain Green's function is given by:

$$\widetilde{G}_{ik}(t) = \sum_{n=1}^{N} \widetilde{G}_{ik}(\frac{b_n}{t})h_n. \tag{7}$$

Here, N is the filter length, h_n are the filter coefficients, b_n are the filter abscissae and t is the time instant.

Werthmüller et al. (2018) drew the conclusion that a provided 201 point filter is the best one suited to CSEM problems. Consequently, it was decided to use the 201 point filter in this study. A filter is composed of two columns with the same length (number of rows N), the first containing the filter abcissae b, while the second is containing the filter coefficients h. Both values of the abcissae and the coefficients are sorted in an ascending order, with b_{min} and h_{min} as the first elements in the two columns, and b_{max} and h_{max} as the last elements in the same two columns. A short review of the digital filter method can be found in Key (2012).

By applying the digital filter method to equations (4) and (5), the Green's functions are evaluated at the filter abscissae b, making the Fourier transform computationally efficient.

In the initial stage of the digital filter method, a fixed range of logarithmically equidistant frequency samples f_l was generated, with the minimum frequency being equal to

$$f_{l,min} = \frac{b_{min}}{t_{max}},$$

and the maximum frequency

$$f_{l,max} = \frac{b_{max}}{t_{min}}.$$

Here, b_{min} and b_{max} are the smallest and largest abscissae values for a given filter, while t_{min} and t_{max} are the earliest and latest time instants. Subsequently, the Green's function was evaluated for each of these frequencies, the values of which have been used as a basis for interpolation. Then, and according to equation (7), the Green's function was calculated for a new range of frequencies $\hat{f}$,

$$\hat{f} = \frac{b_i}{t_j}, \tag{8}$$

where $i = [0, N]$, $j = [0, M]$, $N = 201$ and M is the number of time samples. These new Green's functions were then spline interpolated during the time-domain transform.

Thus, with obtained realistic source Green's function components in the time-domain $\widetilde{G}_{ik}(\bar{x_r}, t|\bar{x_s})$, and by interpolating the time steps back to linear time, time-domain electric fields for a receiver position $\bar{x_r}$ and given a source position $\bar{x_s}$ can be modeled using equation (3).

It is worth mentioning that $\hat{f}$ presented in equation (8) was restricted to values in the range $[10^{-5}, 3 \cdot 10^3]$ Hz, implying that frequencies below 10^{-5} Hz were extrapolated by responses for $\hat{f} = 10^{-5}$ Hz, while responses for frequencies above $3 \cdot 10^3$ Hz were zeroed out. This is because frequencies below 10^{-5} Hz implies no variation in the responses, while responses for frequencies above $3 \cdot 10^3$ Hz are prone to strong damping, resulting in negligible signals.

Uncertainty

Time-domain sensitivity can now be found using,

$$Sensitivity(t) = \frac{\left|F_{Target}(t) - F_{Background}(t)\right|}{\delta F_{Target}(t)}. \tag{9}$$

Taking a closer look at equation (2) reveals that the uncertainty $\delta F_{Target}(\omega)$ is initially given in the frequency-domain. This means that the uncertainty also has to be transformed to the time-domain before equation (9) can be used to calculate the time-domain sensitivities. Assuming the ambient noise η to be independent of frequency, this can be done simply by inverse Fourier transforming the first term on the right-hand side of equation (2) to the time-domain,

$$\delta F_{target}(t) = \mathfrak{F}^{-1}(\alpha(\omega) F_{target}(\omega)) = (\alpha * F_{target})(t) = \alpha F_{target}(t),$$

where in the convolution (*) α is the relative uncertainty function being a delta function in time, which in the product simply becomes a constant representing the relative uncertainty contribution. The ambient noise constant η can now be included in $\delta F_{Target}(t)$ resulting in the final expression for the experimental uncertainty in the time-domain:

$$\delta F_{Target}(t) = \sqrt{|\alpha E|^2 + |\eta|^2}. \tag{10}$$

RESULTS

Time-domain electromagnetic responses of a 1D stratified offshore subsurface as shown in Figure 1 have been numerically simulated. The main objective of this study is to directly compare the time-domain sensitivities as defined by equation (9) for a horizontal transmitter horizontal receiver configuration on one hand , and a vertical transmitter vertical receiver configuration on the other hand. This is done considering two water depths 270 and 1300 m, representing shallow and deep water environments respectively. In each of the two aforementioned models, a 100 m thick resistor is embedded at four different burial depths Z_r below the seabed. These are 1000 m, 2000 m, 3000 m and 4000 m. In addition, three different offsets X representing near, mid and far fields are modeled. These are 500 m, 3500 m and 6500 m. The resistivities of the different elements of the subsurface are shown in Figure 1.

The source length and current strength of the transmitter modeled are 250 m and 5000 A respectively. In the horizontal configuration, the transmitter lies 0.5 m above the seafloor, whilst in the vertical case, it is elevated 135 and 1165 m from the seafloor, for shallow and deep water respectively. The time-domain source current in equation (3) is step-on step-off, which is switched on 80 s after the onset of the experiment, lasts for 20 s and then is switched off again. The recording time is 200 s, while the listening time is 100 s.

Taking a closer look at equation (10) reveals that representative values for the constants α and η should be determined. The first scales with the electric field, and hence represents the relative uncertainty contribution. The second encompasses uncertainty contributions from the ambient noise. Haland et al. (2012) claimed that electric fields as low as 0.5 nV/m can be resolved, thus, this value is used as the ambient noise level in this study. Two different values for α are determined for the relative uncertainty, these are 1% and 0.14%. The first one is a good estimation for most of the conventional receivers operating today, while the second is more of an ideal but achievable value for static sources and receivers.

By considering different water depths, offsets, burial depths, and relative uncertainties, the goal is to find the optimal combination of these above-mentioned parameters that gives the largest sensitivities in time-domain V-V and H-H methods. Furthermore, patterns in the sensitivities and the electric fields raising from altering these parameters can be observed and discussed. Finally, a conclusion on which configuration is best suited to each of the two water depths is presented. A comprehensive list of all figures and their associated parameters is shown in table 1.

It is worth mentioning that the conclusions presented in this work are made for the time-domain, and hence may be different in the frequency-domain.

Shallow water

Electric fields in time-domain

In the shallow water case, the water depth is 270 m, and the electric field curves in time-domain are shown in Figure 2. The curves represent the logarithm of the absolute values of the vertical and horizontal electric fields for the HC reservoir and the background models.

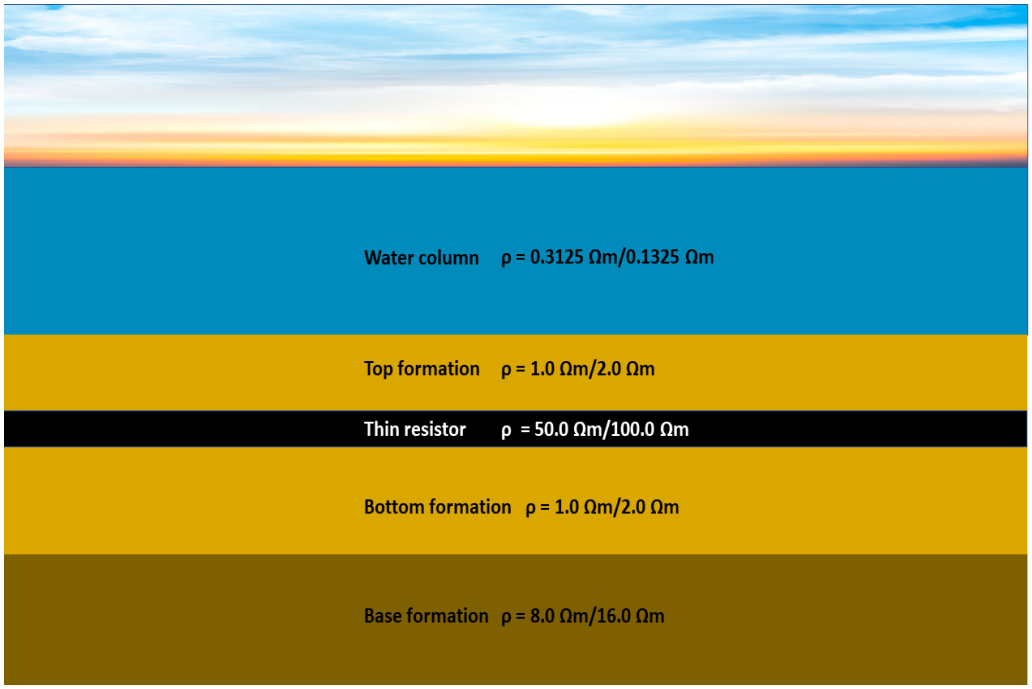

Figure 1: Schematic representation of the subsurface geological plane layer model this study is based upon. Resistivity labels denote horizontal and vertical components.

In plot A, the offset, reservoir depth and relative uncertainty are $X = 500$ m, $Z_r = 1000$ m and $\alpha = 0.01$ respectively. While for plot B, the offset, reservoir depth and relative uncertainty are $X = 6500$ m, $Z_r = 1000$ m and $\alpha = 0.01$ respectively. Note that in plot A for times earlier than 0.1 s, the electric field measured by a horizontal receiver is one order of magnitude stronger than the electric field measured by a vertical receiver. This difference increases with time and becomes two to three orders at times later than 1 s. Considering a larger offset in plot B, it is obvious that the horizontal electric field is several orders of magnitude larger than the vertical one. Additionally, there is a clear difference in the temporal decay of the two curves in plot A, where the vertical electric field decays faster in time than the horizontal. The slope of the vertical electric field becomes steeper with larger offset as shown in plot B, while for H-H it becomes flatter, taking longer time to reach a specified noise floor.

Figure 3, also shows the logarithm of the absolute values of the horizontal and vertical electric fields for the HC reservoir and the background models. In plot A, the offset, reservoir depth and relative uncertainty are $X = 500$ m, $Z_r = 1000$ m and $\alpha = 0.01$ respectively. While for plot B, the offset, reservoir depth and relative uncertainty are $X = 3500$ m, $Z_r = 1000$ m and $\alpha = 0.01$ respectively. Note that in plots A of Figures 2 and 3, a sign reversal of the vertical electric field is taking place at $t = 0.1$ s. This sign reversal moves further in time with offset as shown in plots B, and occurs at about 2.7 s in plot B of Figure 3. On the other hand, no sign reversal is seen for the horizontal electric field. This sign reversal is a well-known feature of time-domain electric fields.

Table 1: Summary table of the key parameters (offset X, burial depth Z_r and relative uncertainty α) pertaining to each presented figure in this work.

Figures	**Offset (X)**	**Burial depth (Z_r)**	**Relative uncertainty (α)**
Figure 2 (A)	500	1000	0.01
Figure 2 (B)	6500	1000	0.01
Figure 3 (A)	500	1000	0.01
Figure 3 (B)	3500	1000	0.01
Figure 4 (A)	500	1000	0.01
Figure 4 (B)	500	2000	0.01
Figure 4 (C)	500	3000	0.01
Figure 4 (D)	500	4000	0.01
Figure 5 (A)	500	1000	0.01
Figure 5 (B)	500	2000	0.01
Figure 5 (C)	500	1000	0.0014
Figure 6 (A)	500	1000	0.01
Figure 6 (B)	500	1000	0.0014
Figure 6 (C)	500	2000	0.01
Figure 6 (D)	500	2000	0.0014
Figure 7 (A)	500	4000	0.01
Figure 7 (B)	3500	4000	0.01
Figure 7 (C)	6500	2000	0.01
Figure 8 (A)	500	4000	0.0014
Figure 8 (B)	3500	4000	0.0014
Figure 8 (C)	6500	4000	0.0014
Figure 9 (A)	500	4000	0.01
Figure 9 (B)	3500	4000	0.01
Figure 9 (C)	6500	4000	0.01
Figure 10 (A)	500	4000	0.0014
Figure 10 (B)	3500	4000	0.0014
Figure 10 (C)	6500	4000	0.0014
Figure 11	500	1000	0.01
Figure 12	500	2000	0.01
Figure 13	500	3000	0.01
Figure 14	500	4000	0.01
Figure 15	3500	1000	0.01
Figure 16	6500	1000	0.01

Sensitivity curves in time-domain

Figure 4 shows the sensitivity curves for four resistor depths: $Z_r = 1000, 2000, 3000$ and 4000 m. The offset and relative uncertainty are similar in all four figures and are set to 500 m and 0.01 respectively. The green and blue lines indicate H-H and V-V sensitivities respectively. The red and green dashed lines indicate the detection and imaging criteria respectively, as defined by Mittet and Morten (2012). This implies that if the scattered field is larger than the experimental uncertainty, i.e., the ratio in equation (9) is larger than one (or larger than

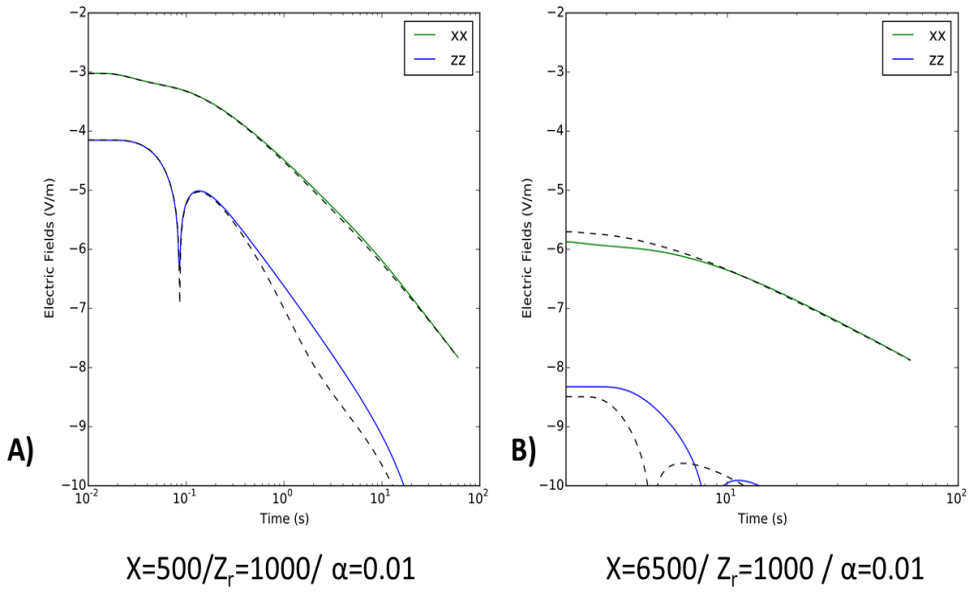

Figure 2: Horizontal (green) and vertical (blue) electric fields in time-domain. The colored lines correspond to background models, while the dashed lines represent the HC reservoir models. Annotations below each plot indicate which offset X, target burial depth Z_r and relative uncertainty α are used to generate the plots. Note that the time axis starts at 0.01 and 2 s in plots A and B respectively. Both axes are logarithmically scaled.

zero in the plot, since the axes are logarithmically scaled), then it is reasonable to assume that the resistive target can be detected, and the sensitivity curve should at least be above the red dashed line (detection criterion). The green dashed line corresponds to one standard deviation from the true transverse resistance of the target, which means that at least 67% of the true transverse resistance of the target can be recovered through imaging, assuming that the sensitivity curve lies above the dashed green line (imaging criterion).
Figure 4 demonstrates that increasing resistor depth does not affect the H-H sensitivity significantly, being able to image resistive targets as deep as 4000 m. On the other hand, the V-V curve shows clear vulnerability with larger burial depths, being unable to image resistors at 4000 m depth below seabed as shown in plot D. Notice the very high V-V sensitivities (spikes) that occur at about 0.1 s. These are a direct consequence of the sign reversal earlier observed in the curves representing vertical electric fields. These sensitivity spikes are resulting from the fact that the time-domain uncertainty $\delta F_{target}(t)$ in equation (10) does not take into account the uncertainty contribution from the derivative of the electric field with respect to time. If $\delta F_{target}(t)$ was to be corrected for that, the sensitivity values at 0.1 s will significantly decrease and the spikes will disappear.

There are three different combinations of offset, target depth and relative uncertainty that result in the V-V sensitivity being higher than the H-H sensitivity. Figure 5 presents these three settings. The first case is shown in plot A, where the offset, reservoir depth and relative uncertainty are $X = 500$ m, $Z_r = 1000$ m and $\alpha = 0.01$ respectively. In plot B, the offset, reservoir depth and relative uncertainty are set to $X = 500$ m, $Z_r = 2000$ m

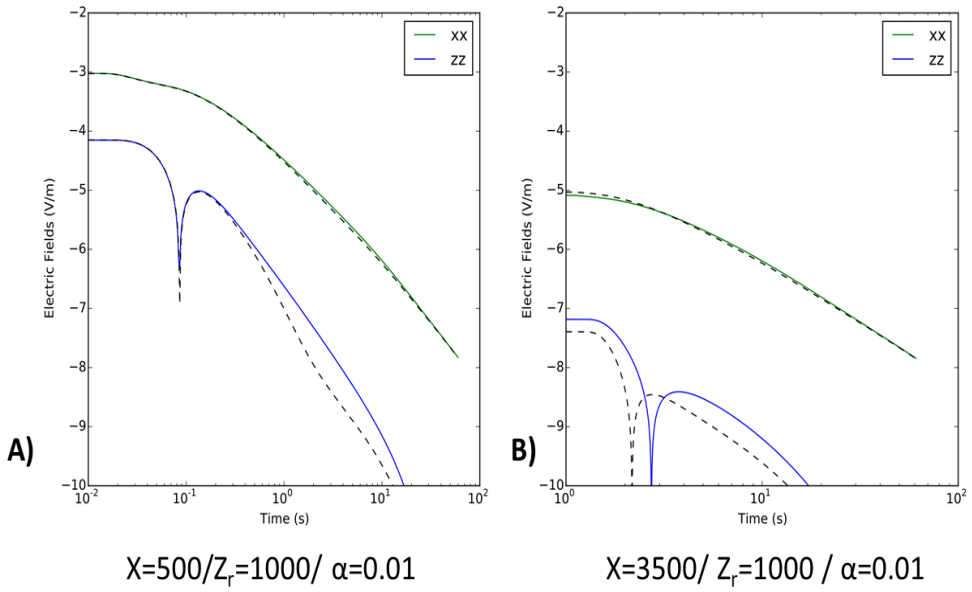

Figure 3: Horizontal (green) and vertical (blue) electric fields in time-domain. The colored lines correspond to background models, while the dashed lines represent the HC reservoir models. Annotations below each plot indicate which offset X, target burial depth Z_r and relative uncertainty α are used to generate the plots. Note that the time axis starts at 0.01 and 1 s in plots A and B respectively. Both axes are logarithmically scaled.

and $\alpha = 0.01$ respectively. Plot C displays the last case, having the offset, reservoir depth and relative uncertainty equal to $X = 500$ m, $Z_r = 1000$ m and $\alpha = 0.0014$ respectively. However, it is worth mentioning that even when the V-V sensitivity is higher than the H-H sensitivity, this does not imply that good imaging results are not achieved solely by relying on the H-H configuration. The H-H green curve is way above the imaging criterion in all three cases.

Next, the focus will be on the impact of reducing the relative uncertainty on the sensitivity curves, while all other parameters will be fixed. Figure 6 shows plots A and B, where the offset and the resistor depth are identical; $X = 500$ m, $Z_r = 1000$ m. The only parameter that is changing from plot A to B is the relative uncertainty α, being 0.01 and 0.0014 in A and B respectively. The dashed black lines and the black arrows highlight the effects introduced by reducing α from plot A to plot B, where the distance between the peaks of the two sensitivity curves is reduced. The variables in plots C and D are the same as A and B, except that the target depth is now changed to 2000 m. It is now clear that simply by reducing the relative uncertainty, the H-H sensitivity technique becomes more sensitive than the V-V technique. Notice that this was intended to solely study the impacts of a reduced relative uncertainty on the sensitivity curves since all curves lie above the imaging limit anyway.

One of the intentions behind modeling an offset equal to 6500 m is to look closer at the airwave presence in the data of the H-H configuration, and to which extent it dominates the reservoir signature. Figure 7 presents three different plots. In plot A, the offset, reservoir

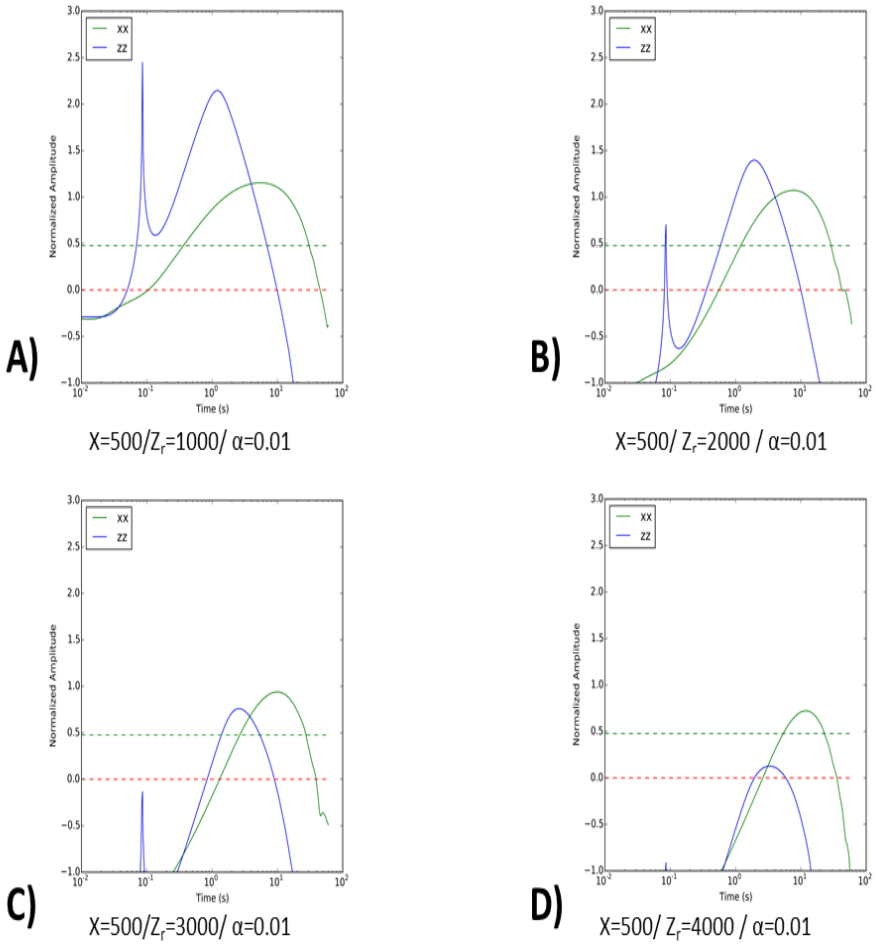

Figure 4: Sensitivity curves in time-domain, found using equation (9). The green curve corresponds to the H-H configuration, while the blue curve represents the V-V configuration. The red dashed line is the detection criteria, while the green dashed line is the imaging criterion. Annotations below each plot indicate which offset X, target burial depth Z_r and relative uncertainty α are used to generate the plots. Both axes are logarithmically scaled.

depth and relative uncertainty are $X = 500$ m, $Z_r = 4000$ m and $\alpha = 0.01$ respectively. The variables of plot B are identical to A except that now, the offset is 3500 m. The offset, reservoir depth and relative uncertainty in plot C are $X = 6500$ m, $Z_r = 2000$ m and $\alpha = 0.01$ respectively. One can spot in plots A and B as highlighted by the red circles, that fairly good H-H sensitivity is achieved down to resistors buried as deep as 4000m. Although the offset is 3500 m in plot B, more than 67% of the true transverse resistance of the target can be imaged. However, once the offset is increased to 6500 m in plot C, the resistor is barely recovered through imaging at 2000 m burial depth as shown by the red circle. This possible masking of the resistor signature can be attributed to the airwave dominance.
Reducing the relative uncertainty in this case results in good H-H sensitivity above the imaging criteria for all three offsets down to 4000 m burial depth as shown in the plots of Figure 8. Here, the variables are identical to those of Figure 7, except that α is now 0.0014. The red circle in plot C of Figure 8 highlights that the possible airwave impact is

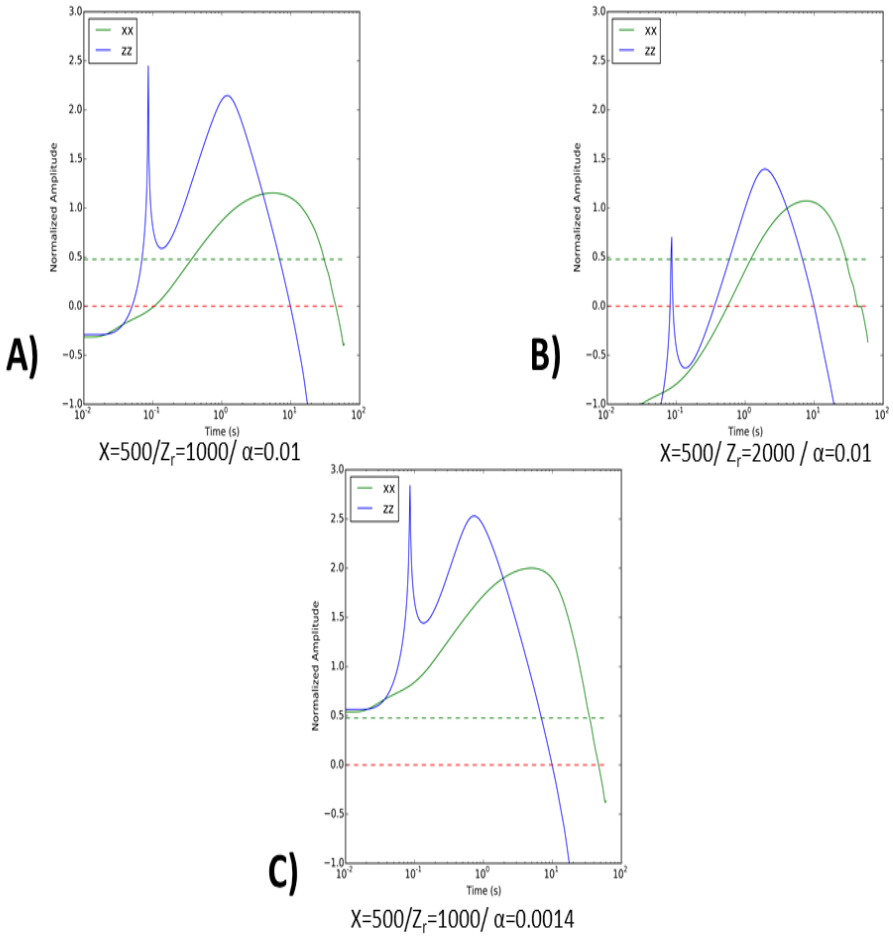

Figure 5: Sensitivity curves in time-domain, found using equation (9). The green curve corresponds to the H-H configuration, while the blue curve represents the V-V configuration. The red dashed line is the detection criteria, while the green dashed line is the imaging criterion. Annotations below each plot indicate which offset X, target burial depth Z_r and relative uncertainty α are used to generate the plots. Both axes are logarithmically scaled.

now minimized, resulting in increased sensitivity for the H-H configuration at 4000 m burial depth.

Deep water

Electric fields in time-domain

The water depth is now set to 1300 m. The same observations can be made on the amplitude differences and sign reversal behaviors of the horizontal and vertical electric fields. These have been presented earlier in this paper in Figures 2 and 3.

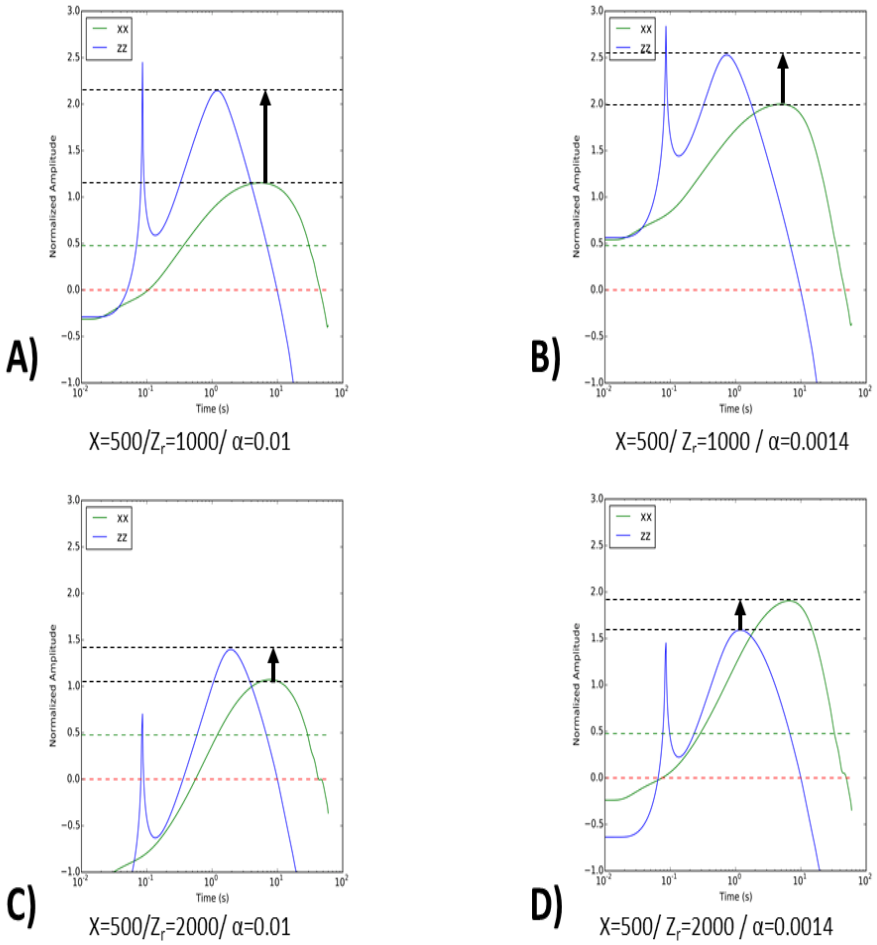

Figure 6: Sensitivity curves in time-domain, found using equation (9). The green curve corresponds to the H-H configuration, while the blue curve represents the V-V configuration. The red dashed line is the detection criteria, while the green dashed line is the imaging criterion. Annotations below each plot indicate which offset X, target burial depth Z_r and relative uncertainty α are used to generate the plots. The black dashed lines and arrows highlight the outcomes of reducing the relative uncertainty from 0.01 to 0.0014. Both axes are logarithmically scaled.

Sensitivity curves in time-domain

Figure 9 includes three plots. The reservoir depth and relative uncertainty are the same in all three plots and are $Z_r = 4000$ m and $\alpha = 0.01$ respectively. The offsets in plots A, B and C are 500, 3500 and 6500 m respectively. Figure 9 shows that both the H-H and V-V sensitivity curves lie below the imaging criterion (green dashed line) in all three plots, and are hardly detectable in plot A since they barely plot over the detection criterion (red dashed line). In plot C, none of the methods show ability in detecting the resistor.
Figure 10 displays the same figures but now with a smaller relative uncertainty α. The H-H sensitivity curve is now clearly above the imaging criterion when the offset is either 500 or 3500 m. For offsets equal to 6500 m, the resistive target is at least detectable compared to the case with a larger α. Note that reducing the relative uncertainty here has no significant effect in improving the sensitivity of the V-V method.

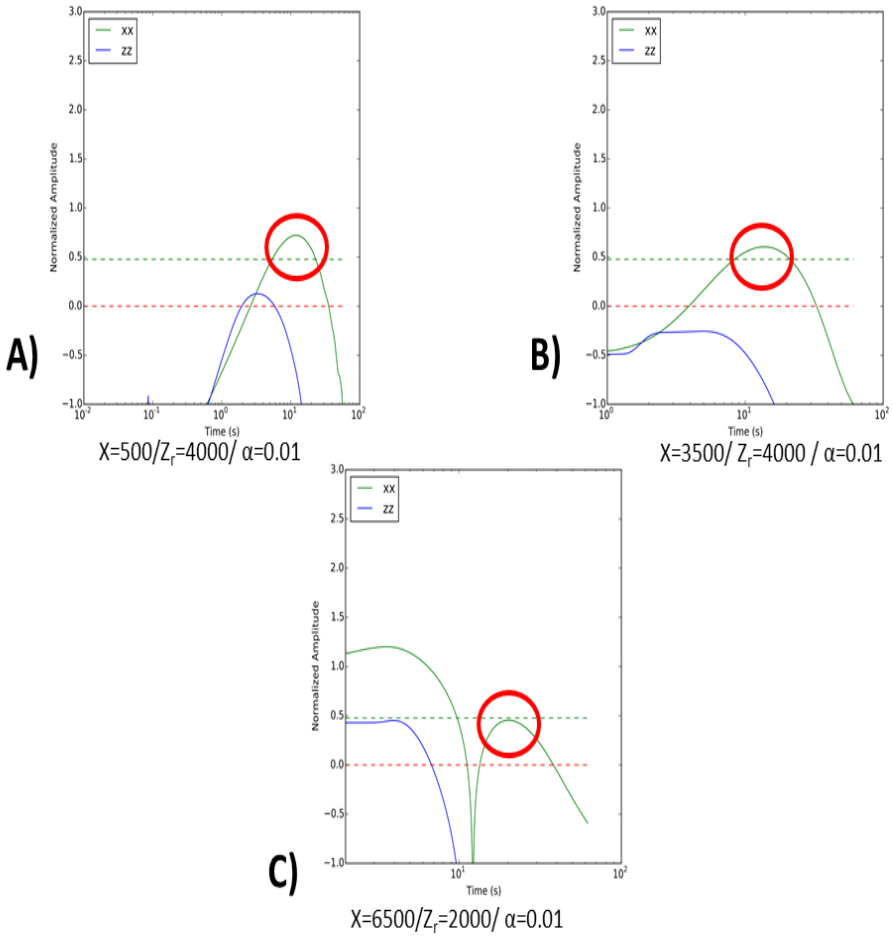

Figure 7: Sensitivity curves in time-domain, found using equation (9). The green curve corresponds to the H-H configuration, while the blue curve represents the V-V configuration. The red dashed line is the detection criteria, while the green dashed line is the imaging criterion. Annotations below each plot indicate which offset X, target burial depth Z_r and relative uncertainty α are used to generate the plots. The red circles highlight the part of the H-H sensitivity curves where the airwave is assumed to be observable in reducing the sensitivity when the offset is 6500 m. Note that the time axis starts at 0.01, 1 and 2 s in plots A, B and C respectively. Both axes are logarithmically scaled.

Shallow vs. deep water

Near offsets

Both the shallow and deep water cases display the better performance of the V-V configuration compared to the H-H in terms of sensitivity to HC targets, assuming small offsets ($\sim$ 500 m) and slightly shallow burial depths ($\sim$ 2000 m). Figure 11 demonstrates this for the shallow water and the deep water cases, both with the same parameters, where the offset, target depth and relative uncertainty are set to $X = 500$m, $Z_r = 1000$ m and $\alpha = 0.01$ respectively. The same can be observed in Figure 12, where the burial depth is now changed to 2000 m.
It will be entirely focused on the currently available limit value for the relative uncertainty:

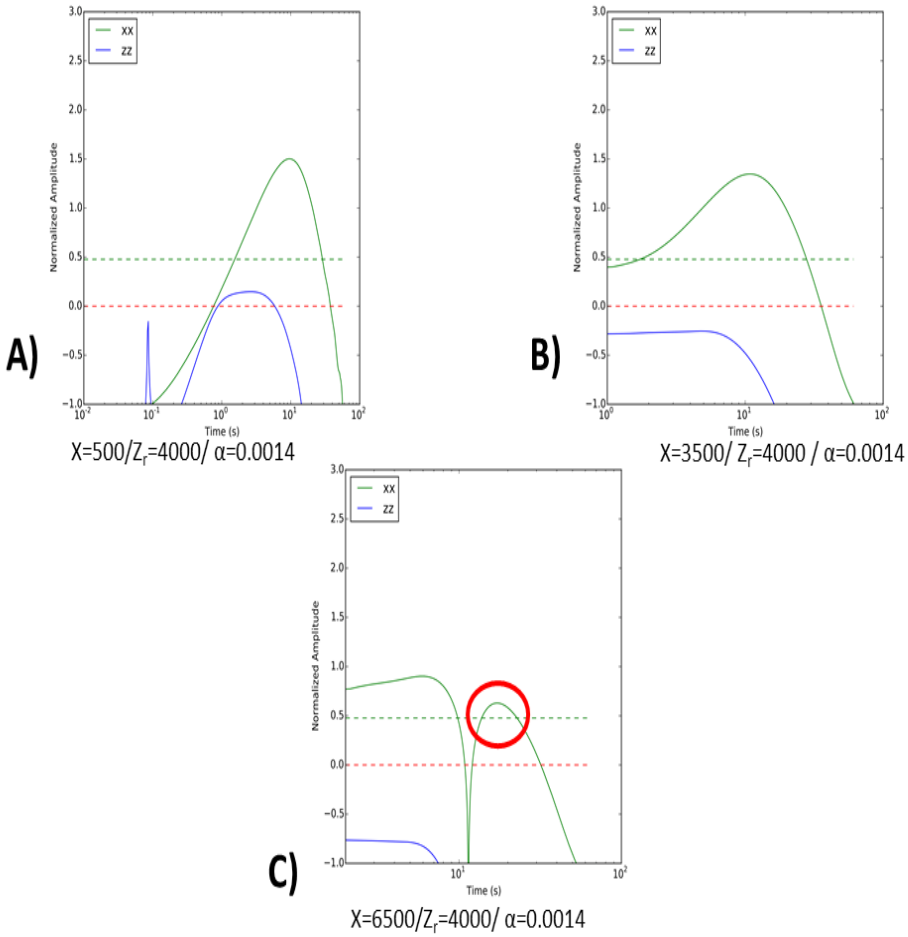

Figure 8: Sensitivity curves in time-domain, found using equation (9). The green curve corresponds to the H-H configuration, while the blue curve represents the V-V configuration. The red dashed line is the detection criteria, while the green dashed line is the imaging criterion. Annotations below each plot indicate which offset X, target burial depth Z_r and relative uncertainty α are used to generate the plots. The red circle highlights the part of the H-H sensitivity curve where the airwave impact is now minimized since $\alpha = 0.0014$. Note that the time axis starts at 0.01, 1 and 2 s in plots A, B and C respectively. Both axes are logarithmically scaled.

$\alpha = 0.01$, bearing in mind from the earlier results that reducing α has the greatest impact for the H-H configuration. The reason for this will be presented later in the discussion section.

Further, considering larger target burial depths, the situation becomes different, where a shift in the behaviors of V-V sensitivity in shallow water is spotted. Figure 13 shows that the H-H configuration is now more sensitive in the shallow water case when $Z_r = 3000$, while it is the V-V that is more sensitive in the deep water case. Taking into consideration a reservoir buried at 4000 m depth in Figure 14, the H-H technique becomes the suitable one in shallow water, while both methods do fail in imaging the target in deep water.

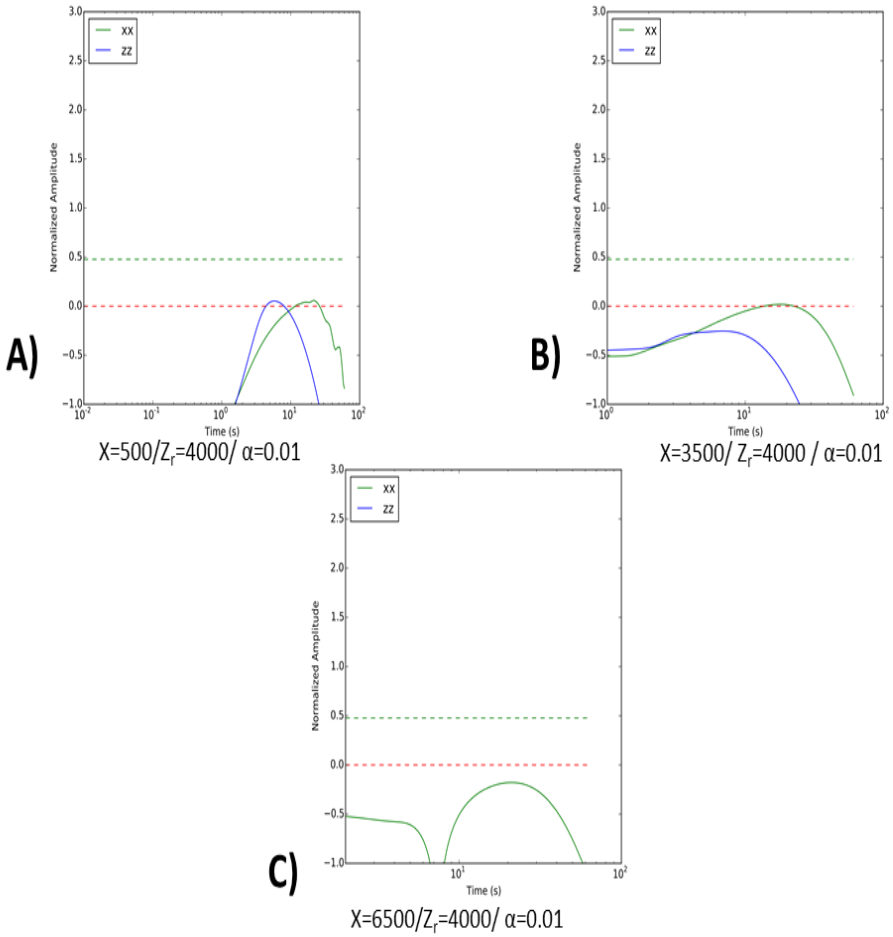

Figure 9: Sensitivity curves in time-domain, found using equation (9). The green curve corresponds to the H-H configuration, while the blue curve represents the V-V configuration. The red dashed line is the detection criteria, while the green dashed line is the imaging criterion. Annotations below each plot indicate which offset X, target burial depth Z_r and relative uncertainty α are used to generate the plots. Note that the time axis starts at 0.01, 1 and 2 s in plots A, B and C respectively. Both axes are logarithmically scaled.

Mid-offsets

It is accepted as a fact that the H-H configuration favors mid to far offsets ($\sim$ 3500 m), due to the physics pertaining to the geometrical setup of the experiment. However, in shallow waters, larger offsets can be prone to prominent airwave signatures masking the diagnostic reservoir responses. In Figure 15, shallow and deep water models generated for offset, resistor depth and relative uncertainty being equal to $X = 3500$m, $Z_r = 1000$ m and $\alpha = 0.01$ respectively are shown. The same pattern seen in Figure 13 is once again observed in Figure 15. The red circles highlight the interesting portions of the curves, where the H-H method is well above the imaging criterion in the shallow water case and is clearly more sensitive than V-V. Moving to the deep water model, the trend shifts, and the V-V curve is the single one lying above the imaging criterion. Burying the target 1000 m deeper to 2000 m burial depth, the same observations can be made for both water depth models.

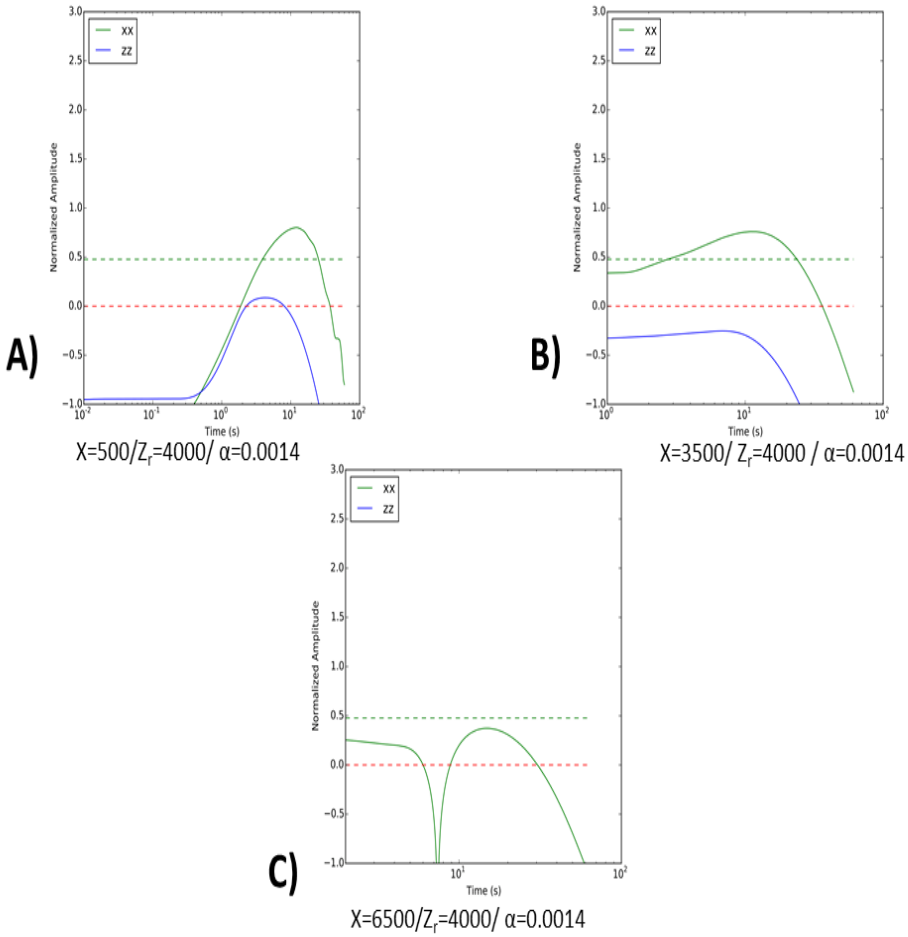

Figure 10: Sensitivity curves in time-domain, found using equation (9). The green curve corresponds to the H-H configuration, while the blue curve represents the V-V configuration. The red dashed line is the detection criteria, while the green dashed line is the imaging criterion. Annotations below each plot indicate which offset X, target burial depth Z_r and relative uncertainty α are used to generate the plots. Note that the time axis starts at 0.01, 1 and 2 s in plots A, B and C respectively. Both axes are logarithmically scaled.

As soon as the reservoir depth becomes 3000 m, the V-V sensitivity drops significantly below the imaging limit in both water depth models. Increasing the burial depth further to 4000 m, causes it to drop even further below the detection limit. On the other hand, it is only in the shallow water case where the H-H sensitivity curve lies above the imaging criterion for both 3000 and 4000 m target depths.

Far offsets

The offset considered here is $X = 6500$ m. Figure 16 presents the shallow and deep water sensitivity curves for a target buried at 1000 m depth. The V-V configuration in shallow water shows no sensitivity, while the H-H method is hardly above the imaging limit as indicated by the red circle. In deep water, no configuration is enabling successful target imaging. The slightly good sensitivity of H-H in shallow water decreases gradually with

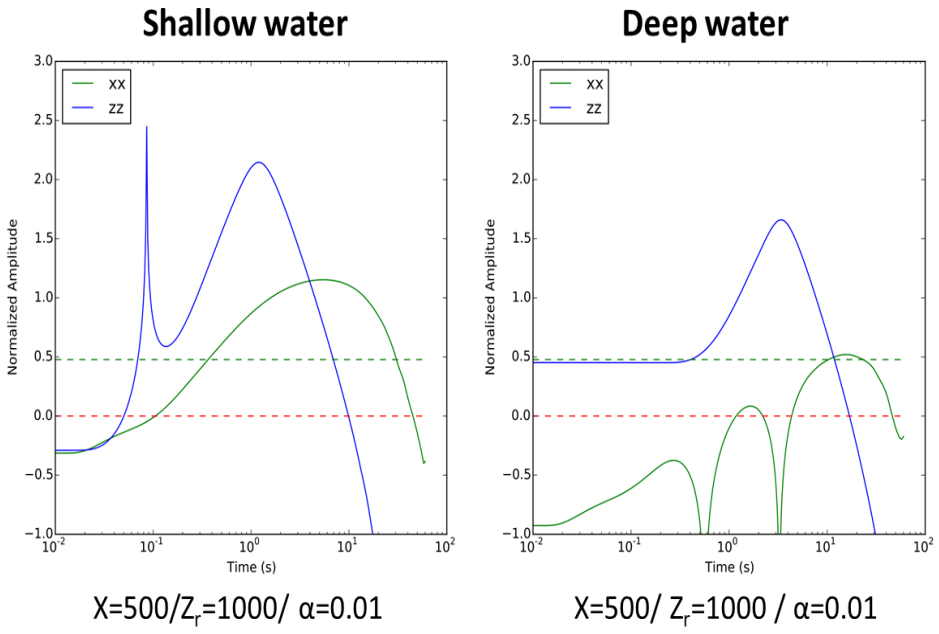

Figure 11: Shallow and deep water sensitivity curves in time-domain, found using equation (9). The green curve corresponds to the H-H configuration, while the blue curve represents the V-V configuration. The red dashed line is the detection criteria, while the green dashed line is the imaging criterion. Annotations below each plot indicate which offset X, target burial depth Z_r and relative uncertainty α are used to generate the plots. Both axes are logarithmically scaled.

target burial depth, making it a real challenge to image resistive targets at depths larger than 1000 m.

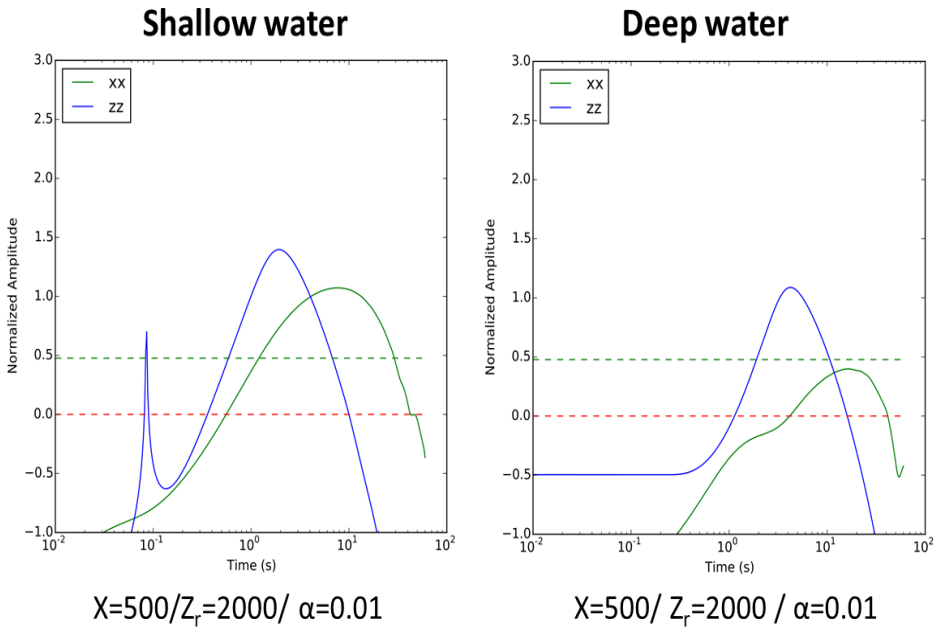

Figure 12: Shallow and deep water sensitivity curves in time-domain, found using equation (9). The green curve corresponds to the H-H configuration, while the blue curve represents the V-V configuration. The red dashed line is the detection criteria, while the green dashed line is the imaging criterion. Annotations below each plot indicate which offset X, target burial depth Z_r and relative uncertainty α are used to generate the plots. Both axes are logarithmically scaled.

DISCUSSION

In this paper, time-domain electromagnetic responses of a 1D plane layer offshore subsurface have been simulated, considering two different transmitter and receiver configurations, and two different water depths among other parameters. The objective is to directly compare the time-domain sensitivities defined by equation (9) earning valuable insight into which configuration is best suited to each of the two water depths.

Electric fields in shallow and deep water environments

It is obvious from Figures 2 and 3 that vertical electric fields have significantly smaller magnitudes than horizontal electric fields, and this conforms with the theory and earlier observations on the subject matter. This amplitude difference can reach orders of magnitude with later times and larger offsets implying that the horizontal electric fields can tolerate higher background noise levels. Also, the horizontal scattered fields are much larger than the vertical resulting in higher sensitivities assuming identical background noise uncertainties. However, it should be stressed that the relative uncertainty term in equation (10) scales with the amplitude of the electric field, meaning that if the electric field amplitude increases, the relative uncertainty will also increase. The H-H configuration shows considerably longer decay times, using longer time to reach a specified noise floor, with the caveat that the relative uncertainty will also be significant since it scales with the electric field. The observed

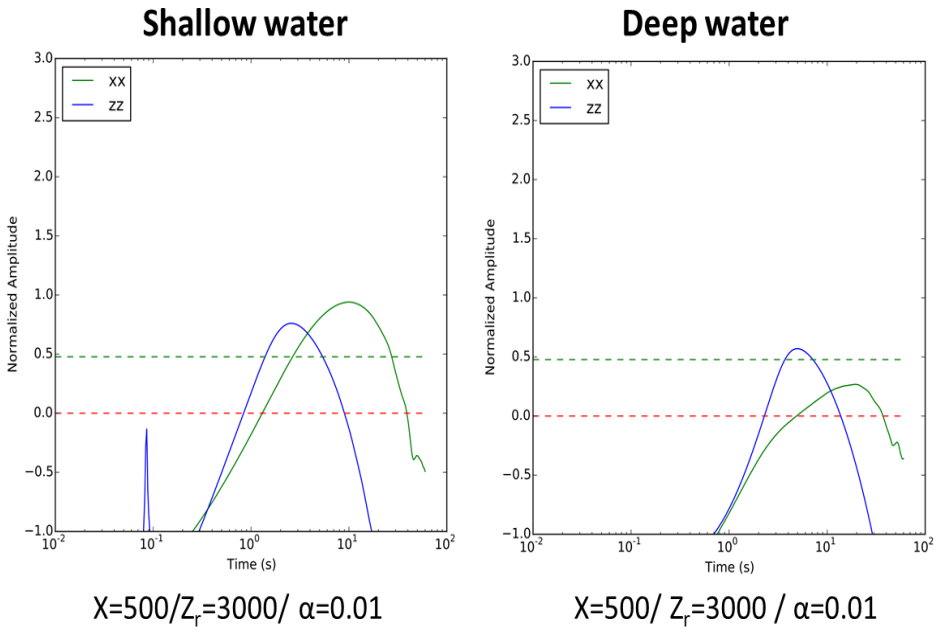

Figure 13: Shallow and deep water sensitivity curves in time-domain, found using equation (9). The green curve corresponds to the H-H configuration, while the blue curve represents the V-V configuration. The red dashed line is the detection criteria, while the green dashed line is the imaging criterion. Annotations below each plot indicate which offset X, target burial depth Z_r and relative uncertainty α are used to generate the plots. Both axes are logarithmically scaled.

sign reversal in the vertical electric fields is due to the fact that the electric fields become negative in value, and since their absolute values are being plotted, the sign reversal will appear as a result.

Shallow Water

Figure 4 shows that the H-H configuration is able to image deeply buried resistive targets in shallow water environments, in contrast to the V-V configuration which is restricted to shallow targets. This is supported by the results of Figure 5, where it is shown that the most optimal settings for the V-V configuration to be more sensitive than the H-H are small offsets around 500 m and fairly shallow resistors not deeper than 2000 m. The fact that resistive targets deeper than 2000 m are challenging conforms with results presented in Weiss (2007).

Figure 6 proves that reducing the relative uncertainty α has the greatest impact for H-H, and the reason for this can be seen in equation (10), where α is scaled with the electric field. Since the horizontal electric field is earlier shown to be many orders of magnitude larger than the vertical, a smaller α will significantly reduce the ratio in equation (9) in the horizontal case compared with the vertical one.

At large offsets about 6500 m in shallow waters, the airwave effect should be taken into account when considering the H-H configuration, this is especially true if one wants to image targets deeper that 2000 m, as shown in plot C of Figure 7. A reasonable way to

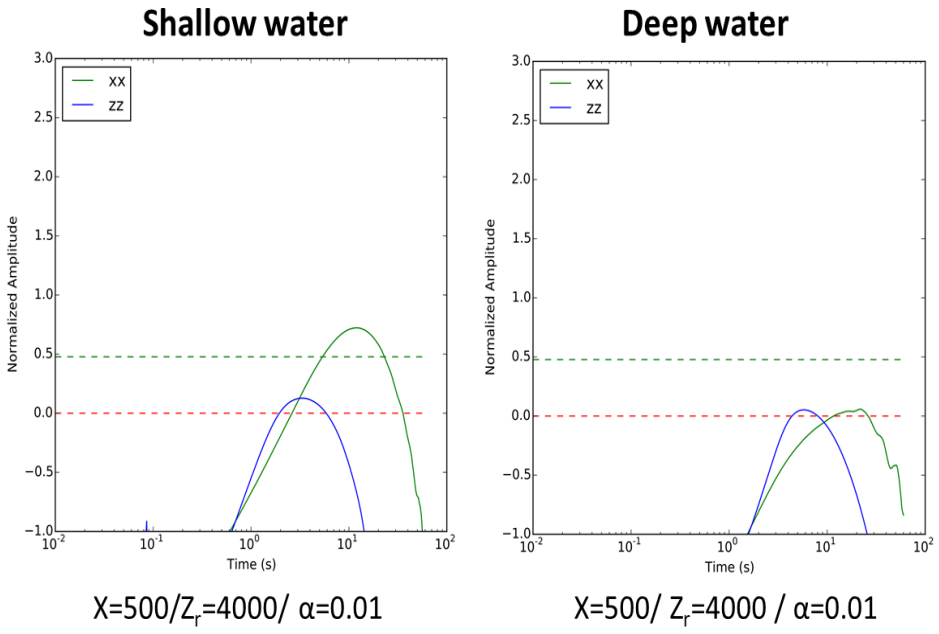

Figure 14: Shallow and deep water sensitivity curves in time-domain, found using equation (9). The green curve corresponds to the H-H configuration, while the blue curve represents the V-V configuration. The red dashed line is the detection criteria, while the green dashed line is the imaging criterion. Annotations below each plot indicate which offset X, target burial depth Z_r and relative uncertainty α are used to generate the plots. Both axes are logarithmically scaled.

circumvent the possible issue of the airwave is by increasing the sensitivity by reducing the relative uncertainty, as presented in plot C of Figure 8, where target recovery through imaging is achieved at 4000 m burial depth.

Deep water

Both configurations tend to fail in detecting deep resistors at 4000 m burial depth in deep waters as shown by Figure 9. Target imaging under these conditions is not feasible. However, by reducing the relative uncertainty to 0.0014 in Figure 10, target imaging is possible for offsets up to 3500 m using the H-H configuration. And at least, good detectability can be achieved when the offset is 6500 m for the same configuration. However, based on the observations made from Figures 9 and 10, the V-V method does not seem to be able to image deep targets in deep water environments, and a limited degree of detectability can be achieved assuming small offsets about 500 m.

Shallow vs. deep water

Near offsets

Considering what has been presented so far, it is clear by now that the V-V configuration is the most optimal for small offsets, regardless of whether the water depth is shallow or deep.

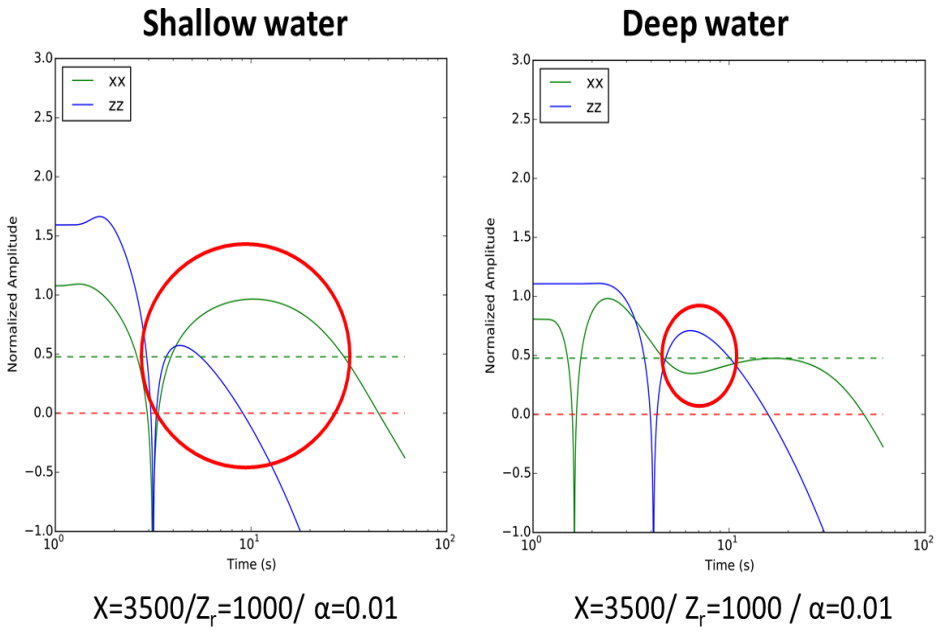

Figure 15: Shallow and deep water sensitivity curves in time-domain, found using equation (9). The green curve corresponds to the H-H configuration, while the blue curve represents the V-V configuration. The red dashed line is the detection criteria, while the green dashed line is the imaging criterion. Annotations below each plot indicate which offset X, target burial depth Z_r and relative uncertainty α are used to generate the plots. The red circles indicate the most useful portions of the sensitivity curves in detection and imaging of resistive targets. Both axes are logarithmically scaled.

Jang et al. (2013) have also come to the same conclusion, stating that only short offsets are required for the V-V configuration to be optimal. However, the target depth plays a key role, in the sense that this holds true only for burial depths down to 2000 m. Deeper burial depths limit the V-V method in shallow water as shown in Figures 13 and 14, where the H-H configuration shows higher sensitivity. Moving to the deep water case when $Z_r = 3000$ m, it is the V-V method that makes target imaging possible. However, none of the methods is able to image deep resistors buried at 4000 m in deep waters. In the frequency-domain, these same configurations might yield different results.

Mid offsets

Despite the alleged limitations that can be introduced by the airwave in shallow water for the H-H configuration, Figure 15 proves that it is the H-H method that possesses the highest sensitivity in shallow water, while the V-V tends to favor deep water when larger offset is modeled, and the burial depth is not larger than 2000 m. The fact that the V-V configuration shows higher sensitivities in deep water environments is also supported by Frafjord et al. (2016). Increasing the resistor depth beyond that makes the V-V technique inappropriate for imaging regardless of water depth, and successful imaging can only be achieved in shallow water environments by the H-H configuration.

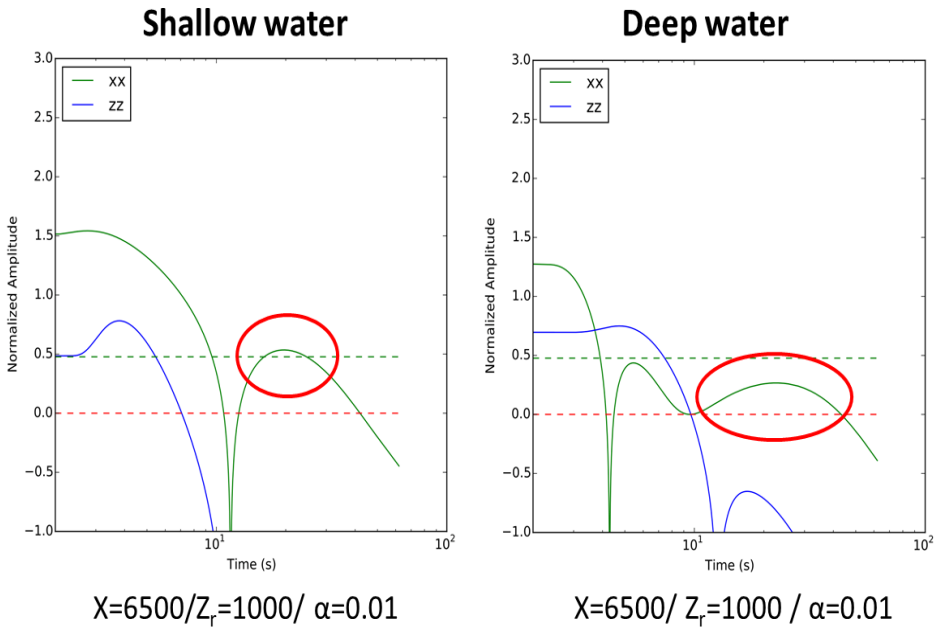

Figure 16: Shallow and deep water sensitivity curves in time-domain, found using equation (9). The green curve corresponds to the H-H configuration, while the blue curve represents the V-V configuration. The red dashed line is the detection criteria, while the green dashed line is the imaging criterion. Annotations below each plot indicate which offset X, target burial depth Z_r and relative uncertainty α are used to generate the plots. The red circles indicate the most useful portions of the sensitivity curves in detection and imaging of resistive targets. Both axes are logarithmically scaled.

Far offsets

The V-V method demonstrates obvious weaknesses when large offsets are encountered in both offshore environments, being unable to even detect the shallowest target that was modeled. On the other hand, the H-H configuration barely allows for target imaging for the shallowest target in shallow water, implying no ability to image targets deeper than that. Also, for the H-H configuration, target imaging in deep water is not an option, and a limited degree of detectability can be achieved down to 3000 m burial depth.

CONCLUSION

In this paper, time-domain 3D electric fields generated by two different acquisition configurations have been simulated in plane layer models, while considering experimental uncertainty. These time-domain electric fields are further employed to investigate and compare the sensitivity of each configuration to thin resistive targets. The first configuration combines vertical transmitters and vertical receivers, while the second combines horizontal transmitters and horizontal receivers. This was done by firstly modeling the EM responses in the frequency-domain. Then, the modeled responses were Fourier transformed into time-domain series by using the method of digital filters. The applied time-domain code uses a step-off waveform current, implying that the primary field is insignificant in the near offsets.

Two water depths were modeled, these are 270 and 1300 m, and the intention is to represent shallow and deep water environments. In each of the two water depth models, a 100 m thick resistor is embedded at four different burial depths below the seabed. Additionally, three different offsets were studied, representing near, mid and far fields.

At the near offset, the vertical transmitter vertical receiver configuration's sensitivity is clearly higher than that of the horizontal transmitter horizontal receiver configuration, regardless of the water depth, and assuming the target is not deeper than 2000 m. This fairly conforms with earlier studies made on this configuration. It should be stressed that even when the horizontal configuration shows less sensitivity than the vertical, this does not imply that reasonable imaging results cannot be achieved solely from the horizontal configuration. However, for a deeper target, the situation becomes water depth dependent. At 3000 m burial depth in deep water, target imaging is only achieved by the vertical configuration, and the horizontal configuration does a better job in shallow water. Burying the target at 4000 m, target imaging is not feasible employing the vertical configuration, and a limited degree of detectability can be observed in both water environments. At mid to far offsets, the vertical configuration shows clear weaknesses, where the sensitivity is significantly decreased compared with near offsets. The feasibility of the vertical configuration at short offsets implies that local geological variations with less 3D effects can be derived by applying the vertical configuration.

Looking at the horizontal configuration, resistive targets at 4000 m burial depth in shallow water can be imaged assuming small to intermediate offsets. However, and since reducing the relative uncertainty has the greatest impact for the H-H configuration, target imaging of resistors at 4000 m can also be possible at the far offset with a reduced relative uncertainty. Moreover, with the currently available value for relative uncertainty, imaging of resistive layers at 4000 m in deep waters is not feasible employing the horizontal configuration. However, simply by the reducing the relative uncertainty, the last-mentioned configuration allows us to image these deeply buried targets up to 3500 m in offset, and a reasonable degree of detectability can be achieved when the offset is 6500 m.

The presented sensitivity analysis can be used in deciding which technique that best suits the water environment under investigation, taking into consideration the optimal combination of offset, target depth and relative uncertainty that will ultimately result in successful target imaging or at least target detection. Additionally, the impacts of a lower relative uncertainty on each configuration have been presented, providing valuable insight into the requirements of next generation CSEM acquisition tools.

ACKNOWLEDGMENTS

This work has been carried out as a part of joint cooperation between the Department of Geoscience and Petroleum at NTNU and Emgs Electromagnetic Geoservices.

I would like to thank Emgs for offering me this opportunity to develop myself as a student, and to be a part of their working environment, by providing me with my own office at the company.

I would like to express my sincere gratitude to my supervisor, Chief Scientist Rune

Mittet for giving me the opportunity to work with this interesting project, but also for his unlimited support and guidance. The feedback and discussions have been essential for the completion of this work, and have definitely developed my understanding of this field. I would also like to wholeheartedly thank R&D Manager Jan Petter Morten for his valuable feedback, support and care while ensuring to include me in the company team.

REFERENCES

Chave, A. D., and C. S. Cox, 1982, Controlled electromagnetic sources for measuring electrical conductivity beneath the oceans: 1. forward problem and model study: Journal of Geophysical Research: Solid Earth, **87**, 5327–5338.

Constable, S., 2010, Ten years of marine csem for hydrocarbon exploration: Geophysics, **75**, 75A67–75A81.

Constable, S., and L. J. Srnka, 2007, An introduction to marine controlled-source electromagnetic methods for hydrocarbon exploration: Geophysics, **72**, WA3–WA12.

Constable, S., and C. J. Weiss, 2006, Mapping thin resistors and hydrocarbons with marine em methods; insights from 1d modeling: Geophysics, **71**, G43–G51.

Cuevas, N. H., and D. Alumbaugh, 2011, Near-source response of a resistive layer to a vertical or horizontal electric dipole excitation: Geophysics, **76**, F353–F371.

Ellingsrud, S., T. Eidesmo, S. Johansen, M. C. Sinha, L. M. MacGregor, and S. Constable, 2002, Remote sensing of hydrocarbon layers by seabed logging (sbl): Results from a cruise offshore angola: The Leading edge, **21**, 972–982.

Frafjord, ., K. Eide, A. El Kaffas, S. Helwig, and T. Holten, 2016, A 2.5d comparison between two csem methods. 78th EAGE Conference and Exhibition 2016.

Ghosh, D. P., 1971, The application of linear filter theory to the direct interpretation of geoelectrical resistivity sounding measurements*: Geophysical prospecting, **19**, 192–217.

Haland, E., E. G. Flekkoy, and K. J. Maloy, 2012, Vertical and horizontal components of the electric background field at the sea bottom: Geophysics, **77**, E1–E8.

Holten, T., E. G. Flekky, B. Singer, E. M. Blixt, A. Hanssen, and K. J. Mly, 2009, Vertical source, vertical receiver, electromagnetic technique for offshore hydrocarbon exploration: First Break, **27**, A93–A97.

Hunziker, J., E. Slob, and W. Mulder, 2011, Effects of the airwave in time-domain marine controlled-source electromagnetics: Geophysics, **76**, F251–F261.

Jang, H., H. Jang, K. H. Lee, and H. J. Kim, 2013, Step-off, vertical electromagnetic responses of a deep resistivity layer buried in marine sediments: Journal of Geophysics and Engineering, **10**.

Key, K., 2012, Is the fast hankel transform faster than quadrature?: Geophysics, **77**, 21–30.

Løseth, L. O., and B. Ursin, 2007, Electromagnetic fields in planarly layered anisotropic media: Geophysical Journal International, **170**, 44–80.

Mittet, R., and J. P. Morten, 2012, Detection and imaging sensitivity of the marine csem method: Geophysics, **77**, E411–E425.

Weiss, C., 2007, The fallacy of the "shallow-water problem" in marine csem exploration: Geophysics, **72**, A93–A97.

Werthmüller, D., K. Key, and E. C. Slob, 2018, A tool for designing digital filters for the hankel and fourier transforms in potential, diffusive, and wavefield modeling: GEOPHYSICS, 1–43.